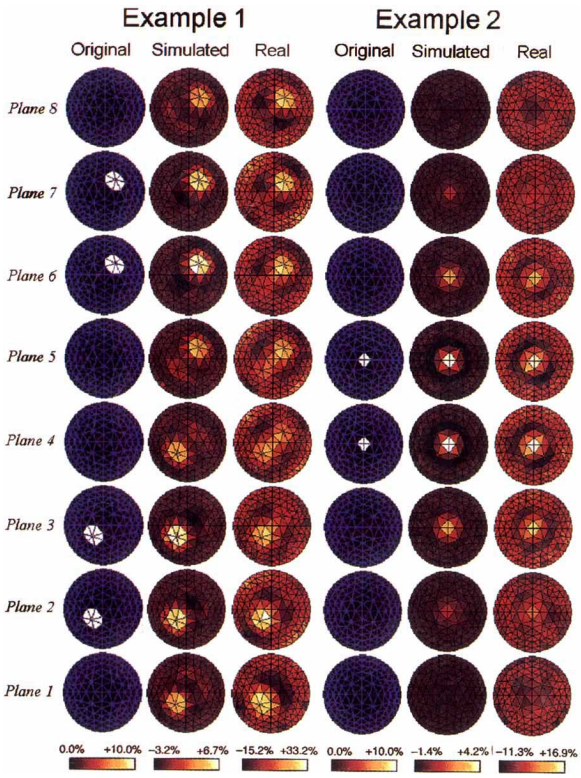

FIG. 4 Comparison of simulated and real images. The original images, of change in conductivity Δc_n, give a representation of nylon cylindrical blocks (diameter 50 mm, length 60 mm) positioned in a saline-filled ($\sigma = 4\,\mathrm{mS\,cm^{-1}}$) phantom. Example 1 corresponds to two blocks located at different heights and radial positions within the phantom. Example 2 corresponds to a single block positioned in the centre of the phantom. Simulated 3D images based on a 1,024 data set give a close representation of the original conductivity distribution with only limited Δc_n changes being propagated into adjacent planes. Real images, reconstructed from data collected from the phantom, are less well defined but the nylon blocks can still be identified.

METHODS. Simulated images are as described in Fig. 3. Real data were collected using a phantom with the same geometrical proportions as the 3D mesh of Fig. 2, using the Sheffield MK3b Electrical Impedance Tomographic Spectroscope (EITS)[16]. This 64-electrode system applies current at eight frequencies over the range 9.6 kHz to 1.2 MHz, and acquires a complete data set in 60 ms. A reference data set was collected from a saline-filled phantom with uniform conductivity. Nylon blocks were then submerged at positions represented by the simulated forward Δc_n image, and another voltage measurement data set was collected. These are normalized to form the boundary data set Δg_n and reconstructed. Images are displayed with colour scales showing the maximum values of percentage conductivity change.

currently implementing a clinical trial to investigate the feasibility of using 3D EIT to detect pulmonary emboli. If the trial is successful, 3D EIT will provide an important alternative to the established radionuclide imaging technique. □

Received 10 October 1995; accepted 23 February 1996.

1. Geddes, L. A. & Baker, L. E. *Med. Biol. Engng* **5,** 271–293 (1967).
2. Duck, F. A. *Physical Properties of Tissue* 167–223 (Academic, London, 1990).
3. Stoy, R. D., Foster, K. R. & Schwan, H. P. *Phys. Med. Biol.* **27,** 501–513 (1982).
4. Pethig, R. *Clin. Phys. Physiol. Meas.* **A8,** 5–12 (1987). **(see note below)**
5. McAdams, E. T. & Jossinet, J. *Physiol. Meas.* **A16,** A1–A14 (1995).
6. Dawids, S. G. *Clin. Phys. Physiol. Meas.* **A8,** 175–180 (1987).
7. Dijkstra, A. M. *et al. J. med. Engng Technol.* **17,** 89–98 (1993).
8. Holder, D. S. & Brown, B. H. in *Clinical and Physiological Applications of Electrical Impedance Tomography* (ed. Holder, D. S.) 47–60 (University College London Press, London, 1993).
9. Barber, D. C., Brown, B. H. & Freeston, I. L. *Electron. Lett.* **19,** 933–935 (1983).
10. Barber, D. C. & Brown, B. H. *J. Phys E: Sci. Instrum.* **17,** 723–733 (1984).
11. Barber, D. C. in *Clinical and Physiological Applications of Electrical Impedance Tomography* (ed. Holder, D. S.) 47–60 (University College London Press, London 1993).
12. Barber, D. C. & Brown, B. H. in *Inverse Problems in Partial Differential Equations* (eds. Colton, D., Ewing, R. Rundell, W.) 151–164 (Soc. for Industrial and Applied Mathematics, Philadelphia, 1990).
13. Rabbani, K. S. & Kabir, A. M. B. H. *Clin. Phys. Physiol. Meas.* **12,** 393–402 (1991).
14. Morucci, J. P., Granié, M., Lei, M., Chabert, M. & Marsili, P. M. *Physiol. Meas.* **A16,** A123–A128 (1995).
15. Goble, J., Chenney, M. & Isaacson, D. *Appl. Comput. Electromagn. Soc. J.* **7,** 128–147 (1992).
16. Brown, B. H. *et al.* (spec. iss. 1) *Innov. Tech. Biol. Med.* **15,** 1–8 (1994).
17. Brown, B. H. & Seagar, A. D. *Clin. Phys. Physiol. Meas.* **A8,** 91–97 (1987).
18. Geselowitz, D. B. *IEEE Trans. biomed. Engng* **18,** 38–41 (1971).
19. Kotre, C. J. *Clin. Phys. Physiol. Meas.* **10,** 275–281 (1989).
20. Barber, D. C. *Clin. Phys. Physiol. Meas.* **10,** 368–370 (1989).
21. Witsoe, D. A. & Kinnen, E. *Med biol. Engng.* **5,** 239–248 (1967).
22. Albert, A. *Regression and the Moore-Penrose Pseudo-inverse* (Academic, New York, 1972).
23. Golub, G. H. & Reinsch, C. *Numer. Math.* **14,** 403–420 (1970).
24. Hansen, P. C. *Numer Alg.* **6,** 1–35 (1994).

ACKNOWLEDGEMENTS. This work was supported by Action Research and EPSRC.

Unrealistic desiccation of marine stratocumulus clouds by enhanced solar absorption

Andrew S. Ackerman & Owen B. Toon

NASA Ames Research Center, National Aeronautical and Space Administration, Moffett Field, California 94035, USA

THE absorption of solar radiation by clouds affects the distribution of heat that drives atmospheric and ocean circulations. Many investigators have measured cloud solar absorption values exceeding theoretical estimates, although the discrepancies have been regarded as inconclusive[1]. But more recent measurements indicate that clouds absorb up to three times as much solar energy than conventional theory predicts[2,3]. Marine stratocumulus clouds are particularly sensitive to solar absorption because marine boundary-layer mixing is typically driven by cloud radiative processes. Here we present model simulations of a stratocumulus-topped marine boundary layer, incorporating different levels of solar absorption. With conventional absorption, the simulations reproduce observed cloud behaviour. But those with artificially enhanced absorption result in an unrealistic daytime depletion of cloud water, because a reduction in cloud radiative cooling results in decreased boundary-layer mixing. Moreover, we show that it is unlikely that liquid water or any plausible dissolved material can absorb the energy required by the recent measurements of solar absorption. Our results therefore indicate that either enhanced solar absorption occurs only in clouds other than marine stratocumulus, or the enhancement of cloud solar absorption indicated by recent measurements[2,3] is overestimated.

Many models of the stratocumulus-topped marine boundary layer show that vertical mixing is driven by radiative cooling near the cloud top[4–10]. These models also show that absorption of solar radiation by clouds can lead to reduced boundary-layer mixing, which restricts the supply of water vapour and results in a daytime thinning of cloud layers. Here we assess the effects of enhanced solar absorption on numerical model simulations of the stratocumulus-topped marine boundary layer, and we address the issue of whether any realistic mechanism can account for the measured enhancement of cloud solar absorption.

To investigate the effects of enhanced solar absorption by clouds, we use a one-dimensional model that treats aerosol and cloud microphysics, radiative transfer and turbulent mixing in the stratocumulus-topped marine boundary layer[10]. With conventional treatment of solar absorption, model-predicted profiles of thermodynamics, cloud microphysics, radiative fluxes and turbulent fluxes compare favourably with airborne measurements of a marine stratocumulus cloud deck[10,11]. Profiles of liquid water are shown in Fig. 1*a*. Vertical mixing was driven primarily by the turbulent buoyancy flux due to radiative cooling near the cloud top

(Fig. 1*b*). The broadband solar absorption for the boundary layer was measured as ~80 W m^{-2}, which exceeded the 53 W m^{-2} predicted by the model; the discrepancy falls within the measurement uncertainties and is primarily due to small differences between the modelled and measured cloud microstructures.

We have explored model sensitivities and found that the model behaves similarly to other one-dimensional models and responds realistically to changes in boundary conditions[10]. Our model results also agree with horizontal averages taken from a three-dimensional simulation of the same stratocumulus deck[12]. Although our model generally reproduces measurements of marine stratocumulus, simplifications are made in a one-dimensional approach. For example, our radiative transfer scheme does not treat broken clouds.

For a baseline case (with conventional solar absorption), we use our model simulation of the marine stratocumulus measured by Nicholls[10,11]. To quantify cloud solar absorption, recent studies have used R, the ratio of cloud shortwave (broadband) radiative forcing at the surface to that at the top of the atmosphere (cloud radiative forcing is defined as the difference between the cloudy and clear-sky net fluxes). To calculate clear sky fluxes we removed all droplets from the model domain at 12:00 (local noon), yielding $R = 1.16$ for the baseline case. This cloud forcing ratio corresponds to an increase in broadband solar absorption for the entire atmospheric column from 216 W m^{-2} in the clear sky to 282 W m^{-2} in the cloudy sky, or 19% to 25%, respectively, of the solar insolation at the top of the atmosphere.

Although this cloud forcing ratio is in the upper range of theoretically expected values[13], some recent measurements indicate that R is much higher, presumably owing to enhanced solar absorption by clouds. Using a global network of surface radiometers and satellite measurements, Cess *et al.*[2] reported an average of $R = 1.5$. But applying the same analysis to a different data set, Li *et al.*[14] found such a large average value in the tropics only. Pilewskie and Valero[3] derived a large value of R (comparable to that reported by Cess *et al.*[2]) using identical radiometers simultaneously flown above and below cloud layers high in the tropical troposphere. In contrast, Hayasaka *et al.*[15] collected similar measurements above and below stratocumulus layers, corrected the measurements for cloud heterogeneity[16], and found no excess cloud absorption.

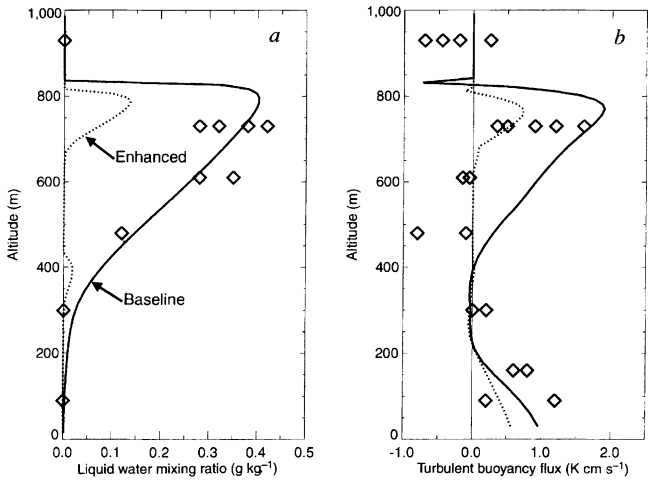

FIG. 1 Comparison between measurements and modelled profiles of liquid water mixing ratio (*a*), and turbulent buoyancy flux (*b*). The diamonds are measurements taken in a stratocumulus deck around noon over the North Sea during July 1982 (ref. 11); the solid (dotted) lines are the model output at 12:00 for the simulation with conventional (enhanced) solar absorption. The model simulations were initialized with cloudless conditions at midnight and run for 24 hours with the observed boundary conditions (during which a persistent cloud layer formed). In additional comparisons, the measured droplet distributions and drizzle fluxes compared favourably with the measurements[10].

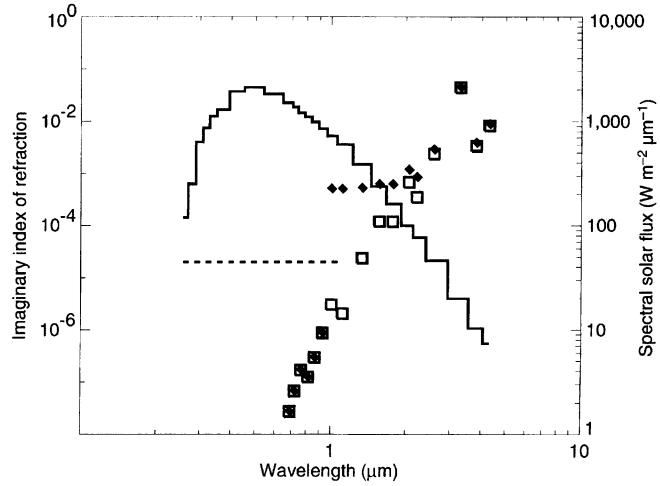

FIG. 2 Imaginary part of the index of refraction for liquid water (left ordinate). Squares, standard values[17–19] used in the model; diamonds, values used in the enhanced simulations; the dashed line is at a value of 2×10^{-5} (equivalent to the minimum value required for a broadband enhancement). For reference the spectral solar flux is overlaid as a solid line (right ordinate).

To enhance solar absorption in our model, we increase the imaginary part of the refractive index of liquid water (k) for wavelengths between 1 and 4.5 μm. We use Mie theory to revise the droplet absorption efficiencies, then recalculate the radiative fluxes for the baseline simulation at noon. To attain $R = 1.5$ with a uniform increase in k between 1 and 4.5 μm requires an addition of 5×10^{-4} to the standard values[17–19] as depicted in Fig. 2. In this case, the cloudy-sky column absorbs 36% of the solar insolation.

Next we run a model simulation starting from a cloudless initial state, but with the revised droplet absorption efficiencies (we will refer to this simply as the 'enhanced simulation'). A comparison of the simulations is shown in Fig. 3. In the baseline simulation, slight minima of cloud water and optical depth occur around noon because solar absorption partially offsets longwave cooling near the cloud top. But in the enhanced simulation, much more pronounced daytime minima develop and persist from about 10:00 to about 18:00 (also evident in the profiles of cloud water in Fig. 1*a*). The cloud layer in the enhanced simulation is depleted of moisture owing to a significant reduction in vertical mixing (Fig. 1*b*), resulting from the enhanced solar absorption. Although the revised droplet optical properties result in $R = 1.5$ for the baseline cloud, in the enhanced simulation the forcing never reaches that value (at noon it is only 1.33) owing to a negative feedback between increased absorption and decreased cloud thickness.

To see if the drastic daytime depletion of cloud water can be avoided, we have evaluated the effects of uncertainties in model inputs. The condensation coefficient describes the fraction of water molecules that stick after impinging on a droplet. Running the enhanced simulation again with a condensation coefficient of 0.035 (rather than 1.0), the cloud layer again thinned drastically. Other input uncertainties include the subsidence rate and the sea surface temperature. We ran three further variations of the enhanced simulation: (1) no subsidence, (2) sea surface temperature increased by 1 K, and (3) no subsidence and the sea surface temperature increased by 1 K. In all three simulations, the cloud layer again thinned drastically. These results verify that the cloud-thinning effects of enhanced solar absorption are robust with respect to model uncertainties.

We have shown that enhanced solar absorption leads to an unrealistic daytime depletion of cloud water; next we explore possible mechanisms for such absorption. The imaginary refractive index of droplets with dissolved absorbing material varies linearly with the molar concentration of the dissolved absorber (this linear variation is commonly used in laboratory studies; its basis is found in the dispersion equations for the dielectric constant[20]). Assuming that the dissolved material is extremely absorbing, so that $k = 1$ at a concentration of 1 M, the molar concentration of a dissolved absorber required to obtain the observed cloud forcing ratio is 5×10^{-4}. However, ionic concentrations in cloud water are generally $<10^{-4}$ M (refs 21 and 22). Exceptions are Cl^-, Na^+, SO_4^{2-} and Mg^{2+} in some marine rainwater samples, and numerous inorganic ions in fogs. So even if we make a very generous assumption about the absorption by dissolved species, they are rarely found in concentrations high enough to provide the required absorption.

Another possibility is that the conventional k values for liquid water are systematically low. The measurement certainties in k are ~10% (refs 17–19), yet increasing k by a factor of 10 results in $R = 1.32$ for the baseline cloud. Hence uncertainties in k cannot account for the recently reported enhancement of solar absorption ($R = 1.5$). But to explore the effects of an intermediate enhancement we ran a simulation with k increased by a factor of 10. The drastic daytime thinning of the cloud layer occurred again but was slightly delayed.

Next we consider a broadband enhancement due to suspended material such as black carbon (properties described in ref. 23). We assume that the carbon is symmetrically distributed as a shell around each water droplet, which maximizes its absorption efficiency (thereby requiring the minimum amount of carbon), and for simplicity we assume a constant volume fraction of carbon in each droplet. Revised scattering and absorption efficiencies are then calculated[24]. To attain $R = 1.5$ in the baseline cloud requires a volume fraction of 4×10^{-5}, which exceeds by orders of magnitude the amounts of black carbon measured in clouds influenced by urban pollution[25] and in rain water affected by biomass burning[26]. Together with a modelled liquid water path of 133 g m^{-2}, the volume fraction requires a black carbon concentration of 6 μg m^{-3} in the boundary layer (all of it in cloud droplets). Such high concentrations are sometimes exceeded in heavily polluted regions, but rareiy so[27]. (For comparison we assumed a fixed volume of carbon in each droplet and repeated the calculation; the same total concentration of carbon was required).

A broadband absorber can also be ruled out by commonplace observations. Prescribing a minimum value of $k = 2 \times 10^{-5}$ for liquid water also yields $R = 1.5$ for the baseline cloud. The transmission of light of wavelength λ through a uniform absorbing layer of thickness h is given by $\exp(-4\pi kh/\lambda)$. Hence a puddle of water 1 cm deep with such absorption would transmit only 1.5% of the incident light at a visible wavelength of 0.6 μm. Clearly, rain water is much more transparent.

We find that there are no plausible mechanisms for cloud water to provide the absorption recently suggested by measurements. The uncertainties in the measured optical constants are insufficient; black carbon is not found in high enough concentrations (except in severely polluted air), and any broadband absorber would violate the commonplace observation that centimetre-thick layers of water are transparent. Also, there are no known dissolved species in water with high enough concentrations to account for the absorption (with the exception of special cases such as fog), even assuming the dissolved species are extremely good absorbers.

Our model results may be related to the shortcomings of our one-dimensional model[10], although we are unaware of any systematic reasons for this to be the case. We recommend that our results be verified with three-dimensional models, but we anticipate that other models of radiatively driven cloud layers will produce similarly unrealistic results with enhanced solar absorption. We therefore conclude that either radiatively driven cloud models are less realistic than previously thought, or that the enhancement of cloud solar absorption indicated by recent measurements has been overestimated or does not apply to marine stratocumulus. □

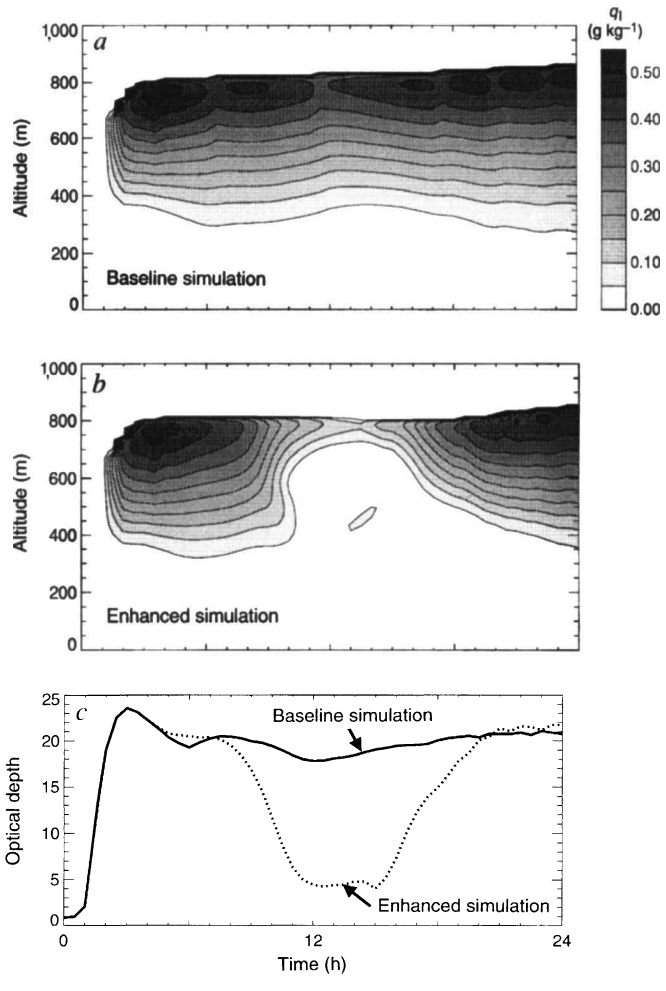

FIG. 3 Evolution of water mixing ratio (q_l, in units of g kg^{-1}) with time for the baseline simulation (*a*) and the enhanced simulation (near-infrared case; *b*). *c*, Evolution of optical depth (at 0.6 μm) of the modelled boundary layers. Line patterns are the same as in Fig. 1. The maxima of liquid water and optical depth at 03:00 in both simulations are due to a burst of boundary-layer mixing caused by cloud formation. A transient lower cloud develops in the enhanced simulation owing to accumulation of vapour in the surface mixed layer.

Received 13 September 1995; accepted 9 February 1996.

1. Stephens, G. L. & Tsay, S.-C. *Q. Jl. R. met. Soc.* **116,** 671–704 (1990).
2. Cess, R. D. *et al. Science* **267,** 496–499 (1995).
3. Pilewskie, P. & Valero, F. P. J. *Science* **267,** 1626–1629 (1995).
4. Lilly, D. K. *Q. Jl. R. met. Soc.* **94,** 292–309 (1968).
5. Bougeault, P. *J. atmos. Sci.* **42,** 2826–2843 (1985).
6. Chen, C. & Cotton, W. R. *J. atmos. Sci.* **44,** 2951–2977 (1987).
7. Turton, J. D. & Nicholls, S. *Q. Jl. R. met. Soc.* **113,** 969–1009 (1987).
8. Duynkerke, P. G. *Mon. Weath. Rev.* **117,** 1710–1725 (1989).
9. Rogers, D. P. & Koracin, D. *J. atmos. Sci.* **49,** 1473–1486 (1992).
10. Ackerman, A. S., Toon, O. B. & Hobbs, P. V. *J. atmos. Sci.* **52,** 1204–1236 (1995).
11. Nicholls, S. *Q. Jl. R. met. Soc.* **110,** 783–820 (1984).
12. Kogan, Y. L., Khairoutdinov, M. P., Lilly, D. K., Kogan, Z. N. & Liu, Q. *J. atmos. Sci.* **52,** 2923–2940 (1995).
13. Chou, M.-D., Arking, A., Otterman, J. & Ridgeway, W. L. *Geophys. Res. Lett.* **22,** 1885–1888 (1995).
14. Li, Z., Barker, H. W. & Moreau, L. *Nature* **376,** 486–490 (1995).
15. Hayasaka, T., Kikuchi, N. & Tanaka, M. *J. appl. Met.* **34,** 1047–1055 (1995).
16. Ackerman, S. A. & Cox, S. K. *J. appl. Met.* **20,** 1510–1515 (1981).
17. Painter, L. R., Birkhoff, R. D. & Arakawa, E. T. *J. chem. Phys.* **51,** 243–251 (1969).
18. Palmer, K. F. & Williams, D. *J. opt. Soc. Am.* **64,** 1107–1110 (1974).
19. Downing, H. D. & Williams, D. *J. Geophys. Res.* **80,** 1656–1661 (1975).
20. Bohren, C. F. & Huffman, D. R. *Absorption and Scattering of Light by Small Particles* Ch. 9 (Wiley, New York, 1983).

21. Galloway, J. N., Likens, G. E., Keene, W. C. & Miller, J. M. *J. geophys. Res.* **87,** 8771–8786 (1982).
22. Warneck, P. *Chemistry of the Natural Atmosphere* 405–406 (Academic, London, 1988).
23. Chylek, P., Ramaswamy, V. & Cheng, R. J. *J. atmos. Sci.* **41,** 3076–3084 (1984).
24. Toon, O. B. & Ackerman, T. P. *Appl. Opt.* **20,** 3657–3660 (1981).
25. Twohy, C. H., Clarke, A. D., Warren, S. G., Radke, L. F. & Charlson, R. J. *J. geophys. Res.* **94,** 8623–8631 (1989).
26. Cachier, H. & Ducret, J. *Nature* **352,** 228–230 (1991).
27. Cachier, H., Brémond, M.-P. & Baut-Ménard, P. *Nature* **352,** 371–373 (1989).

ACKNOWLEDGEMENTS. This work was supported by NASA and the US DOE. A.A. was supported by a Research Associateship from the US National Research Council.

Fluxes of CO_2 and water between terrestrial vegetation and the atmosphere estimated from isotope measurements

Dan Yakir & Xue-Feng Wang

Department of Environmental Sciences and Energy Research, The Weizmann Institute of Science, Rehovot 76100, Israel

The atmospheric budget of carbon compounds can be balanced only by invoking a significant 'missing sink' for carbon dioxide[1–3]. Identifying this sink requires a knowledge of CO_2 fluxes at global and local scales. The former can be estimated from global averages of CO_2 concentration and isotope composition[4–9]; local-scale measurements have been made by analysing individual eddies of air[10,11]. In both cases, the net CO_2 exchange is the sum of two opposing fluxes: uptake by gross primary productivity and release by respiration. Here we show that these two components can be estimated separately at the local scale from small vertical gradients in ^{13}C and ^{18}O in atmospheric CO_2 above vegetation. By also analysing the ^{18}O content of moisture in the air samples, we can estimate evapotranspiration rates, providing information on water exchange between the biosphere and atmosphere[12]. We suggest that this approach can be extended to the regional scale.

Gradients in concentrations and isotopic compositions of CO_2 and water vapour above crop fields were measured with a 12-m mast that enabled measurement of wind speed and sampling of air at several heights above the canopy. Air was sucked either through a CO_2/H_2O infrared gas analyser to determine concentration gradients or through a cold trap and a 2-l flask to obtain samples of water vapour and CO_2 for determination of isotopic gradients. The results of measurements on a sunny midday over a wheat field are shown in Fig. 1. As expected, concentrations of CO_2 decreased, and concentrations of H_2O increased, towards the vegetation because of net photosynthetic CO_2 uptake and evapotranspiration, respectively. Similarly, $\delta^{13}C$ values of the CO_2 increased towards the vegetation because of the discrimination against ^{13}C associated with photosynthetic CO_2 fixation[13], while $\delta^{18}O$ values of the CO_2 increased because of isotopic exchange with ^{18}O-enriched leaf water[7,9,14].

Variations in trace gas concentrations, such as shown in Fig. 1*a*, *f*, have been commonly used to estimate net fluxes between the land surface and the atmosphere[15,16]. This aerodynamic approach relies on the assumption that momentum, heat and mass (of, for example, CO_2 and H_2O) are transported by eddies of turbulent air and therefore behave similarly in this context. Fluxes and gradients can therefore be related by the eddy diffusivity. Although net fluxes can be more directly estimated based on co-variance of vertical wind speed and concentrations in individual eddies of air[11,17], the need for fairly large samples of air for isotopic analysis made the aerodynamic approach more appropriate for the studies reported here. The net fluxes of water vapour and CO_2 were calculated from the gradients according to:

$$J_x = -k\frac{\Delta C_x}{\Delta z} \quad (1)$$

where ΔC_x is the vertical difference in concentration C of a constituent x over the vertical distance Δz in the canopy boundary layer, and k represents the eddy diffusivity of the air calculated from wind speed profiles and surface characteristics. The results for net fluxes of CO_2 and water vapour are given in Table 1. Notably however, it is the gross fluxes that need to be considered for understanding the behaviour of the biological system and its response to environmental change.

The approach used here to partition the net CO_2 flux into its components is based on the assumption that an air sample taken at a height z above the canopy contains a mixture of air from the background atmosphere (indicated by subscript a) with air that has had CO_2 or H_2O added/removed by the surface biological system (b) according to:

$$C_z = C_a - C'_b \quad (2)$$

where a vertical gradient C_z can be converted to a flux (equation (1)). C'_b may (prime indicates a composite value) be further subdivided into respiratory and photosynthetic components of CO_2 and H_2O (discussed below). Owing to isotopic fractionations associated with biological exchange of CO_2 and H_2O, an isotopic mass balance can be approximated by:

$$C_z\delta_z = C_a\delta_a - C'_b\delta'_b \quad (3)$$

where isotopic abundance is represented in the familiar δ notation[18] (which introduces a possible error in the order of 0.01‰ when calculating δ'_b).

The mixing analysis of equations (2) and (3) can be rearranged in a useful way[19] as:

$$\delta_z = \delta'_b + M/C_z \quad (4)$$

where $M = (\delta_a - \delta'_b)C_a$ and the intercept δ'_b can be empirically obtained from a plot of δ_z versus $1/C_z$ (Fig. 1*c*, *e*). Applying this regression analysis to the atmospheric water vapour data (Fig. 1*f*–*h*) yielded an intercept (δ'_b) of −3.7‰, representing the isotopic signature of the evapotranspiration flux. This value is similar to the mean $\delta^{18}O$ value of stem water in the wheat field (-3.1 ± 0.3‰, $n = 14$) as indeed is required by the widely made assumption of isotopic steady-state of leaf water (during which the $\delta^{18}O$ values of input (stem) water, and output (transpired) water vapour are equal[14,20]). Consistency with the regression analysis was also found for the CO_2 results.

The biological flux of CO_2, with an isotopic signature δ'_b, is composed of respiratory (r) and photosynthetic (p) components that can be independently estimated. Considering their specific isotopic signatures in the context of equation (3) leads to:

$$C_z\delta_z = C_a\delta_a - C_p\delta_p + C_r\delta_r \quad (5)$$

Equation (5) can be solved for C_p and (because $C'_b = C_p - C_r$,) for C_r. Using these values, together with estimates of the eddy diffusivity, the gross photosynthetic and respiratory fluxes, J_p and J_r respectively, can now be calculated (see equation (1)) according to:

$$J_p = -k\frac{\Delta C_p}{\Delta z} = -k\frac{\Delta C'_b}{\Delta z}f_1 \quad (6)$$

and

$$J_r = -k\frac{\Delta C_r}{\Delta z} = -k\frac{\Delta C'_b}{\Delta z}f_2 \quad (7)$$

where $f_1 = (\delta'_b - \delta_r)/(\delta_p - \delta_r)$ and $f_2 = (\delta'_b - \delta_p)/(\delta_p - \delta_r)$. Notably, the δ values used in the equations above represent either $\delta^{18}O$ or $\delta^{13}C$, each dominated by different processes and yielding independent estimates of J_p and J_r.

To apply the above approach at the field scale, we characterized the isotopic signatures of the CO_2 associated with photosynthesis,